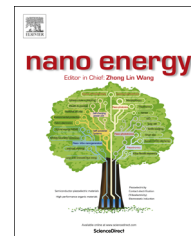


Available online at www.sciencedirect.com

ScienceDirect

journal homepage: www.elsevier.com/locate/nanoenergy

RAPID COMMUNICATION

Template-grown graphene/porous Fe₂O₃ nanocomposite: A high-performance anode material for pseudocapacitors



Jizhang Chen^a, Junling Xu^a, Shuang Zhou^a, Ni Zhao^{a,*},
Ching-Ping Wong^{a,b,**}

^aDepartment of Electronic Engineering, The Chinese University of Hong Kong, New Territories, Hong Kong

^bSchool of Materials Science and Engineering, Georgia Institute of Technology, Atlanta, GA 30332, United States

Received 16 April 2015; received in revised form 21 May 2015; accepted 21 May 2015

Available online 9 June 2015

KEYWORDS

Iron oxide;
Hierarchical structure;
Porous structure;
Graphene;
Nanocomposite;
Asymmetric
supercapacitor

Abstract

Composition design and morphology control can lead to high performance electrode materials for energy storage devices. In this work a graphene/porous Fe₂O₃ nanocomposite anode material is fabricated via a template-assisted nanocasting process. This nanocomposite consists of graphene scaffold with high electronic conductivity and interconnected Fe₂O₃ with porous structure, thus exposing ample active sites for redox reactions and offering sufficient contacts with the electrolyte. Owing to these morphological advantages, the nanocomposite outperforms nearly all the reported Fe-based anode materials by delivering a high specific capacitance of 1095 F g⁻¹ at a current density of 3 A g⁻¹. In addition, the material shows great rate capability and good cycling stability. Asymmetric supercapacitors are fabricated by assembling the graphene/porous Fe₂O₃ nanocomposite (as the anode material) with a CoNi-layered double hydroxide/carbon nanotube composite (as the cathode material). The devices exhibit high energy and power densities of 98.0 W h kg⁻¹ and 22,826 W kg⁻¹, which are among the best performances reported to date for asymmetric supercapacitors.

© 2015 Elsevier Ltd. All rights reserved.

*Corresponding author. Tel.: +852 3943 4347.

**Corresponding author at: Department of Electronic Engineering, The Chinese University of Hong Kong, New Territories, Hong Kong. Tel.: +852 3943 8447.

E-mail addresses: nzhao@ee.cuhk.edu.hk (N. Zhao),
cwpwong@cuhk.edu.hk (C.-P. Wong).

Introduction

Supercapacitors with notable features such as high power density and long-term cyclability are emerging as a promising energy storage device for hybrid electric vehicles, load

leveling, back-up power systems, etc. [1-3]. Currently, the supercapacitor market is dominated by electric double layer capacitors (EDLCs) using porous carbon as both anode and cathode materials. These devices, however, suffer from low energy density that hinders their applications [4-9]. To overcome this obstacle, extensive research efforts have been devoted to explore pseudocapacitive materials, namely, transition metal (Ni, Co, Mn, Ru, etc.) oxides, hydroxides and sulfides. These pseudocapacitive materials store charges via Faradaic redox reactions and could therefore possess much higher specific capacitances than porous carbon that stores charges via physical adsorption [10-20]. So far the pseudocapacitive materials are primarily researched as cathode materials for aqueous asymmetric supercapacitors (ASCs). Owing to their ability of suppressing oxygen evolution, the pseudocapacitive cathodes allow extension of the open-circuit potential from ~ 1 V (for aqueous EDLCs) to ~ 1.6 V (for aqueous ASCs), leading to enhanced energy density. To further improve the performance of ASCs, it is now important to explore alternative anode materials.

An ideal anode material should not only possess proper redox potential but also offer excellent electronic and ionic transport properties, which are critical to the power and energy density of supercapacitors. Redox reactions only occur at the surface and near-surface region of pseudocapacitive materials, while the interior bulk of the materials oftentimes remains inactive due to their poor electronic and ionic conductivities. This is the reason why experimentally measured capacitance values of pseudocapacitive materials are often much lower than the theoretical ones. To effectively enhance the utilization of pseudocapacitive materials, three strategies have been proposed. The first strategy is to employ nanostructures in order to create sufficient surface active sites [21-24]. The second strategy extends the first one by introducing a porous morphology, which render large interfacial contact with the electrolyte and thus allow fast ionic transfers [25-27]. The third approach is to build heterostructured composite materials by integrating pseudocapacitive materials with conductive skeletons (e.g., nano-carbon, graphene) [28-33]. This approach could in principle provide efficient pathways to transport electrons, thus reducing electrochemical polarization and enhancing pseudocapacitive kinetics. Nevertheless, such scenario can only be achieved if the nano-morphology of the composites can be well controlled.

In this work, we designed, fabricated and characterized a hierarchical graphene/ Fe_2O_3 nanocomposite consisting of interconnected Fe_2O_3 with porous structure anchored on the graphene scaffold (hereafter denoted as G- Fe_2O_3). Combining advantages of the above-mentioned strategies, this nanocomposite material exhibits much higher capacitance than most of reported Fe-based pseudocapacitive materials (e.g., Fe_2O_3 nanotubes [11], FeOOH nanosheets [34], Fe_3O_4 nanoparticles [35], C/ Fe_xO_y nanocomposites [36,37], graphene/ Fe_xO_y composites [38-42]). Moreover, a full ASC is assembled by using this material and a CoNi-layered double hydroxide (LDH)/carbon nanotube (CNT) composite as the anode and cathode materials, respectively. The device exhibits a high energy density of 98.0 W h kg^{-1} at a power density of 465.9 W kg^{-1} . Remarkably the energy density of the ASC maintains as high as 25.0 W h kg^{-1} when the power

density reaches $13,832 \text{ W kg}^{-1}$, making the device one of the best performed ASCs reported to date.

Experimental section

Synthesis of graphene/porous Fe_2O_3 nanocomposite

100 mg Graphene oxide (GO, see the synthesis in Supporting Information) was dispersed into 80 mL mixed solution of deionized (DI) water and absolute ethanol (1:1 in volume) containing 500 mg cetyl trimethyl ammonium bromide (CTAB). After being sonicated for 0.5 h, the solution was added by 0.75 mL concentrated ammonia solution (28 wt%). Then this solution was added by 0.64 mL tetraethylorthosilicate (TEOS) and stirred strongly for 5 h. Subsequently, black powers (GO/ SiO_2) were centrifugated out, washed with DI water and dried at 80°C in air. Then, GO/ SiO_2 was treated at a high temperature of 800°C under an Ar atmosphere for 3 h, to be converted to graphene/ SiO_2 nanocomposite. Next, 120 mg graphene/ SiO_2 was added to 10 mL ethanol containing 300 mg $\text{Fe}(\text{NO}_3)_3 \cdot 9\text{H}_2\text{O}$, and then stirred at 50°C until ethanol was evaporated. The obtained black powers were calcined in a furnace at 350°C for 4 h, followed by washing with 1 M NaOH aqueous solution at 80°C and DI water at room temperature completely. Finally, graphene/ Fe_2O_3 nanocomposite was obtained by centrifugation and drying, and is designated as G- Fe_2O_3 . For comparison, D- Fe_2O_3 was obtained by directly calcining iron nitrate in air at 350°C for 4 h. P- Fe_2O_3 was produced by a same process of G- Fe_2O_3 except for the atmosphere of heat treating GO/ SiO_2 (air for P- Fe_2O_3).

Characterization

The XRD patterns were collected using a Rigaku (RU300) diffractometer with Cu $K\alpha$ radiation source ($\lambda=0.1540598 \text{ nm}$). The morphologies were characterized by a field emission scanning electron microscope (FE-SEM, Quanta F400). A Tecnai Spirit Transmission electron microscope (TEM) was used to further investigate the morphology and structure of the sample. High-resolution TEM images and energy dispersive X-ray spectroscopy (EDX) maps were taken by a Tecnai F20 microscope equipped with a HAADF detector for scanning TEM (STEM) and an EDX detector. Raman spectra were recorded with a Renishaw RM-1000 Micro Raman Spectrometer. Investigations of the chemical composition were performed using X-ray photoelectron spectroscopy (XPS, Physical Electronics PHI 5600). N_2 adsorption/desorption measurement was carried out by Micromeritics ASAP 2010 instrument. ICAP6300-type inductively coupled plasma (ICP) spectrometer (Thermo, USA) was used to analyze the Fe content in our sample, and Q5000IR thermogravimetric analyzer (TGA, TA Instruments, USA) was used to obtain the carbon content by heating our sample in air from 50°C to 800°C at a heating rate of $10^\circ\text{C min}^{-1}$.

Electrochemical measurements

Nickel foam was used as the current collector for both positive and negative electrodes. Typically, slurry of 80% active material, 10% carbon black (Super-P) and 10% polyvinylidene difluoride (PVDF) in N-methylpyrrolidone was coated onto nickel foams and then dried at 110°C under vacuum for 12 h. The mass

loading of active materials ranged from 2 to 4 mg cm⁻² for all samples. The obtained electrodes were pressed at 5 MP before electrochemical tests. Three-electrode measurements were performed using the obtained electrode, Pt plate, Hg/HgO electrode and 3 M KOH aqueous solution as working electrode, counter electrode, reference electrode and electrolyte, respectively. Cyclic voltammetry (CV) and galvanostatic tests were conducted at different scan rates and current densities (based on the total mass of active materials) on a CHI 660E electrochemical workstation. Electrochemical impedance spectroscopy (EIS) measurements were carried out with frequency ranging from 10 mHz to 100 kHz and the amplitude being set as 5 mV. For the two-electrode measurements, G-Fe₂O₃, CoNi-LDH/CNT and 3 M KOH aqueous solution served as negative electrode material, positive electrode material and electrolyte, respectively, and were assembled into 2016-type ASC coin cells. Prior to the assembly of ASCs, the masses of G-Fe₂O₃ and CoNi-LDH/CNT were balanced according to: $q_+ = -q_-$. CV and galvanostatic tests were carried out at different scan rates and current densities (based on the total mass of G-Fe₂O₃ and CoNi-LDH/CNT).

Results and discussion

Synthesis and characterization

The precursor exfoliated graphene oxide was synthesized from graphite flakes by a modified Hummers method [43,44]. The

schematic for fabricating G-Fe₂O₃ is described in Figure 1. In step I, porous SiO₂ was anchored onto the graphene scaffold by a solution method using cetyl trimethyl ammonium bromide (CTAB) as the pore former and tetraethylorthosilicate (TEOS) as the Si source, followed by calcination at high temperature under inert atmosphere. Fe₂O₃ was then pulled into pores of SiO₂ in step II through a nanocasting process. The final product, graphene/porous Fe₂O₃ nanocomposite (G-Fe₂O₃), is formed after etching SiO₂ with NaOH. The crystal structure of G-Fe₂O₃ was identified by XRD and the resultant pattern is shown in Figure 2a. G-Fe₂O₃ consists of three phases, namely, graphene, hematite α -Fe₂O₃ (JCPDS 33-0664), and maghemite γ -Fe₂O₃ (JCPDS 25-1402). The existence of carbon in G-Fe₂O₃ is further evidenced by Raman spectrum showing typical D and G bands (Supporting Information, Figure S1). In the XRD pattern, the broadness and low intensity of the Fe₂O₃ peaks imply a low degree of crystallinity of Fe₂O₃ in G-Fe₂O₃. In contrast, the XRD peaks of D-Fe₂O₃ (a control sample obtained by directly calcining iron nitrate in air at 350 °C for 4 h) are relatively sharp and intense, and can be readily assigned to the α -Fe₂O₃ phase. The mean crystal size of Fe₂O₃ in D-Fe₂O₃ is calculated to be 24.6 nm according to the Scherrer equation, in comparison with 3.3 nm in G-Fe₂O₃. Since it is hard to distinguish γ -Fe₂O₃ from Fe₃O₄ using the XRD characterization, we performed XPS analysis to further confirm the chemical composition and purity of G-Fe₂O₃. As shown in Figure 2b, the full survey spectrum is dominated by the signals from Fe, O and C elements; no Si peaks can be seen, suggesting that the SiO₂ template is effectively removed. The high-resolution XPS

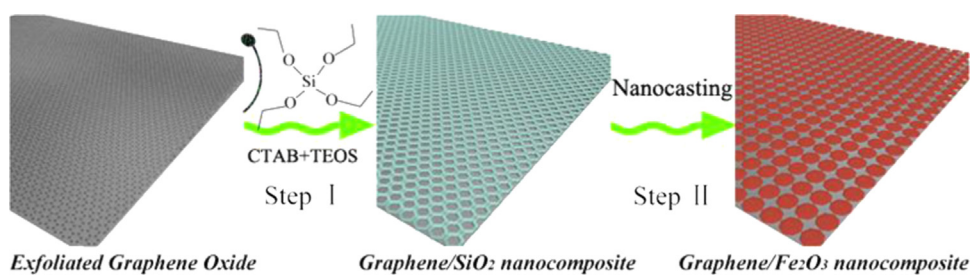


Figure 1 Schematic for the fabrication process of G-Fe₂O₃.

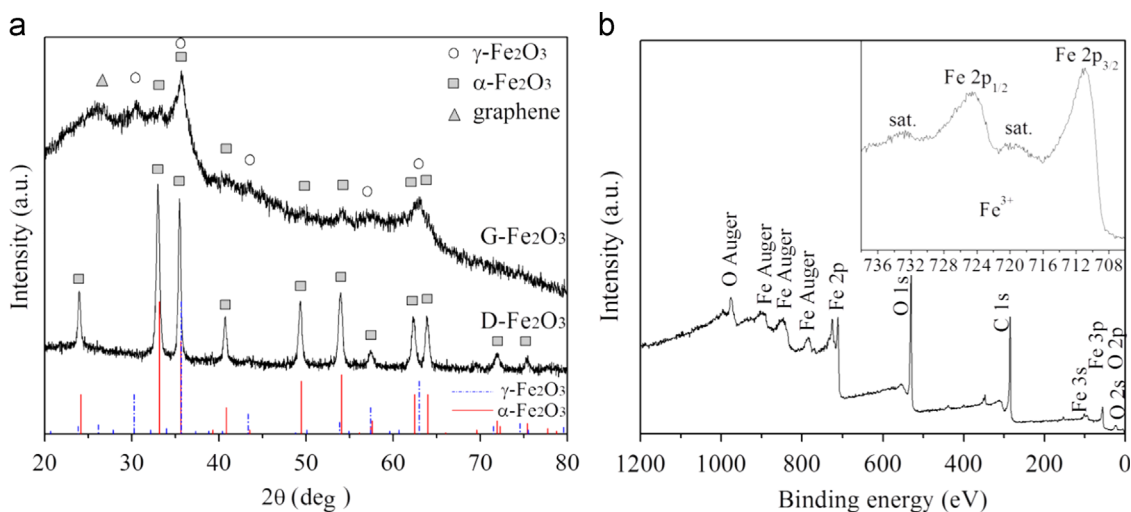


Figure 2 (a) XRD patterns of D-Fe₂O₃ and G-Fe₂O₃. (b) XPS spectrum of G-Fe₂O₃ with the inset showing high-resolution Fe 2p region.

spectrum for the Fe 2p core level (inset of Figure 2b) shows two distinct peaks located at 711.0 and 724.6 eV, corresponding to a spin-orbit couple of Fe 2p_{3/2} and Fe 2p_{1/2}, respectively. In addition, these two peaks are accompanied by two shake-up satellites situated at 719.2 and 732.5 eV, representative of the Fe (III) valence state [45,46]. This result indicates that G-Fe₂O₃ contains no or only trace amount of Fe₃O₄. The high-resolution C 1s spectrum (Supporting Information, Figure S2a) can be deconvoluted into three subpeaks, indicative of C-C/C=C, O-C-O and O-C=O bonds. The predominant intensity of the C-C/C=C peak implies efficient conversion of GO precursor to graphene.

An important advantage of the present method to produce G-Fe₂O₃ is that it easily achieves well-dispersed Fe₂O₃ tiny nanoparticles through the usage of the SiO₂

template. The SEM images of neat graphene (G-ne) and graphene/SiO₂ are shown in Figure S3a-f (Supporting Information), suggesting that SiO₂ was anchored on the surface of graphene nanosheets homogeneously. Consequently, the template-grown G-Fe₂O₃ nanocomposite adopts a uniform morphology, as confirmed by both the SEM and TEM images (Figure 3). The rough surface in Figure 3a indicates that Fe₂O₃ is casted onto the surface of graphene, while Figure 3b demonstrates that Fe₂O₃ clusters disperse uniformly without aggregation. Higher magnification TEM images in Figures 3c and S4 demonstrate that the Fe₂O₃ clusters are composed of nanoparticles, which are interconnected with each other to form porous structure. It is also noted that the size of these Fe₂O₃ nanoparticles is ~5 nm. From N₂ adsorption/desorption measurement (see

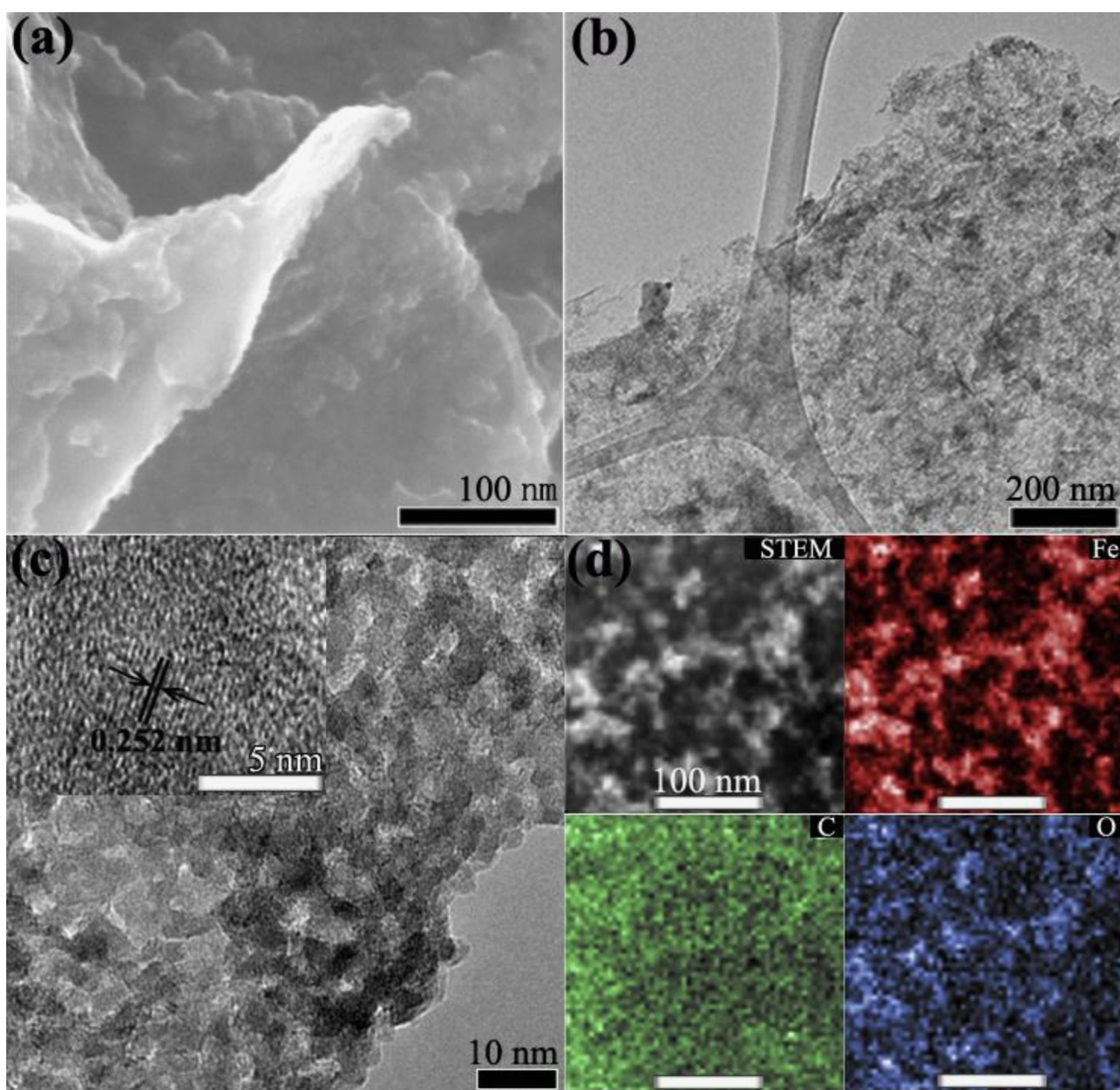


Figure 3 Microscopic characterizations of G-Fe₂O₃: (a) SEM image, (b, c) TEM images, (d) STEM image and EDX elemental maps for C, Fe and O taken from the same zone with the scale bar being 100 nm.

Figure S5), the pore volume and the average pore size in G-Fe₂O₃ are determined to be 0.228 cm³ g⁻¹ and 3.7 nm, respectively. The inset of Figure 3c shows the high-resolution (HR) TEM image of G-Fe₂O₃, which exhibits fringes with a lattice spacing of 0.255 nm, in agreement with the (119) plane of γ -Fe₂O₃ or (110) plane of α -Fe₂O₃. We further employed scanning transmission electron microscopy (STEM) and energy-dispersive X-ray spectroscopy (EDX) mapping to study elemental distribution in G-Fe₂O₃, as shown in Figure 3d. From STEM image and Fe, O and C maps, we can clearly see that C is everywhere, representing the graphene scaffold, while Fe and O (Fe₂O₃) only partially cover the graphene surface due to the use of SiO₂ template. Based on EDX analysis (see Figure S6), the atomic percentages of C, O and Fe atoms are 47.47%, 32.37% and 20.16%, respectively, that is, the weight ratio of Fe₂O₃ is around 72.7% in G-Fe₂O₃. In addition, inductively coupled plasma (ICP) analysis and thermogravimetric analysis (TGA, see Figure S7) have been conducted, and the weight ratio of Fe₂O₃ is determined to be 69.2% and 67.5%, respectively, in good agreement with EDX analysis.

Three-electrode electrochemical measurements

In order to correlate the morphological characteristics of the nanocomposite with its electrochemical performance, we performed cyclic voltammetry (CV) and galvanostatic measurements in a three-electrode setup (Figure S8) in 3 M KOH aqueous electrolyte. Figure 4a shows CV curves of G-Fe₂O₃. The profiles are quite different from the ideal rectangular shape of EDLCs, implying that the energy storage process is dominated by Faradaic redox reactions. At the low scan rate of 5 mV s⁻¹, G-Fe₂O₃ exhibits an anodic peak at -0.578 V and a cathodic peak at -1.055 V, corresponding to the redox process. At 10 mV s⁻¹, the cathodic peak becomes indistinct, while the anodic peak shifts to -0.555 V. As the scan rate is further increased to 50 mV s⁻¹, the anodic peak was broadened. These phenomena are caused by electrochemical polarization, that is, the transports of electrolyte ions and electrons in or close to the active material cannot be synchronized with the rapid

transfer of electrons in the external circuit, and as a result the accumulated electrons on the electrode would increase potential for charging and decrease potential for discharging. Figure 4b compares CV curves of G-Fe₂O₃, P-Fe₂O₃ (a control sample produced also by the nanocasting process but has no graphene scaffold), D-Fe₂O₃ and graphene nanosheet (G-ne) at 5 mV s⁻¹. Among them, D-Fe₂O₃ yields a negligible integrated area due to its large particle size. The P-Fe₂O₃ curve shows an area slightly less than G-Fe₂O₃. The cathodic peak of P-Fe₂O₃ cannot be observed, and its anodic peak locates at -0.562 V that is 0.016 V higher than that of G-Fe₂O₃. This increased difference between cathodic and anodic peaks in P-Fe₂O₃ is likely to originate from the low electronic conductivity of Fe₂O₃, which hinders electronic transports and thus enhances polarization. Evidently the introduction of graphene scaffold in G-Fe₂O₃ reduces such effect.

Galvanostatic curves of G-Fe₂O₃ at different current densities are presented in Figure 5a, showing distinct charging and discharging plateaus. These plateaus are associated with the pseudocapacitive characteristic of Fe₂O₃ and are consistent with the CV curves. In addition, charging and discharging curves are approximately symmetric throughout all current densities, revealing great redox reversibility of G-Fe₂O₃. Galvanostatic curves of G-Fe₂O₃, P-Fe₂O₃, D-Fe₂O₃ and G-ne at 3 A g⁻¹ are shown in Figure 5b for comparison. Similar to the CV results, G-Fe₂O₃ shows the most developed plateaus. The plateaus are situated in -0.70 V for charging and -0.94 V for discharging, with a ΔE of 0.24 V, smaller than the 0.27 V for P-Fe₂O₃. This result further validates higher polarization in P-Fe₂O₃ where the sluggish electronic transport sets a barrier for redox reactions of Fe₂O₃ with the electrolyte ions. In the case of D-Fe₂O₃, plateaus are indistinct, indicating severe polarization due to the large micro-scale particle size. Unlike Fe₂O₃, G-ne shows typical triangle shape of EDLCs. A more detailed set of CV and galvanostatic curves of P-Fe₂O₃, D-Fe₂O₃ and G-ne at various rates are shown in Figure S9. In respect of the pseudocapacitive mechanism of Fe₂O₃, it is commonly ascribed to the reversible conversion of Fe³⁺ to Fe²⁺ accompanied by the intercalation of electrolyte cations [11,36,47]. Recently,

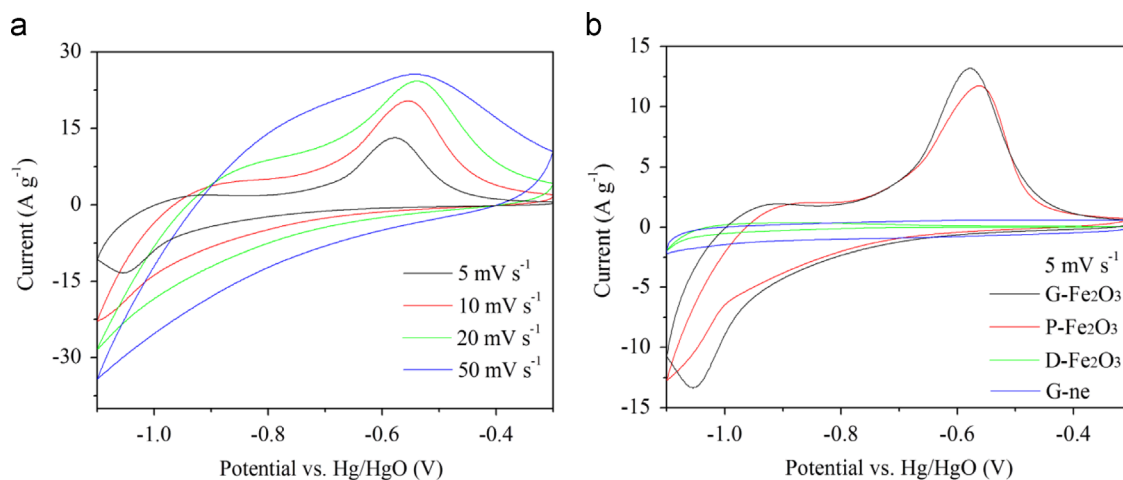
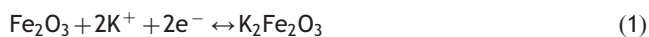


Figure 4 (a) CV curves of G-Fe₂O₃ at different scan rates. (b) Comparative CV curves of G-Fe₂O₃, P-Fe₂O₃, D-Fe₂O₃ and G-ne at 5 mV s⁻¹.

this speculation is evidenced by in situ X-ray absorption spectroscopy (XAS) [34], ex situ XRD and Raman [48], and ex situ XPS measurements [49]. Based on these studies, the charge storage process of Fe_2O_3 in the KOH electrolyte can be described as



Since this process is associated with the diffusions of K^+ and e^- within Fe_2O_3 , the particle size of Fe_2O_3 must be as small as possible to ensure high capacitances at high rates.

A great advantage of the G- Fe_2O_3 electrode is its high capacitance and rate capability. The capacitance values of all the samples are calculated based on the charging curves and are summarized in Figure 5c (see Supporting Information for the calculation procedure). At 3 A g^{-1} , the capacitance of G- Fe_2O_3 is 1095.0 F g^{-1} , higher than 908.2 F g^{-1} of P- Fe_2O_3 and much higher than those of G-ne and D- Fe_2O_3 . Even at a very high rate of 30 A g^{-1} , G- Fe_2O_3 still provides a high capacitance of 506.6 F g^{-1} , which is 5, 11 and more than 500 times of P- Fe_2O_3 , G-ne and D- Fe_2O_3 at 30 A g^{-1} , respectively, implying again that the ionic diffusion and electronic transport in the G- Fe_2O_3 /electrolyte system are much more efficient than its counterparts. The cycling performances of these samples were also evaluated, as shown in Figure 5d. After 1000 cycles, G-ne

remains high capacitance retention of 91.1%, while P- Fe_2O_3 shows poor electrochemical stability. As for G- Fe_2O_3 , it retains 72.3% after 1000 cycles, superior to P- Fe_2O_3 . This is due to the employment of graphene scaffold, which not only offers a highly conductive path, but also functions as a supporting layer to accommodate volumetric expansions of Fe_2O_3 and therefore can prevent Fe_2O_3 from decaying during long cycles. We also note that G- Fe_2O_3 shows the highest capacitance among all the iron based pseudocapacitive materials summarized in Table 1. Such a high capacitance of G- Fe_2O_3 is ascribed to the following three facts. Firstly, graphene scaffolds facilitate electronic transports to the active sites on Fe_2O_3 . Secondly, the tiny particle size of Fe_2O_3 ensures sufficient surface area for redox reactions. Last, the pores among Fe_2O_3 provide extensive contacts with the electrolyte ions [25-27,50]. Moreover, electrochemical impedance spectroscopy (EIS) measurements (Figures S10 and S11) were used to demonstrate the superiority of G- Fe_2O_3 with low charge transfer impedance, high knee frequency, and low phase angle in comparison with the counterparts.

Asymmetric supercapacitors

To further explore the potential of G- Fe_2O_3 as an anode material, we have fabricated asymmetric supercapacitors

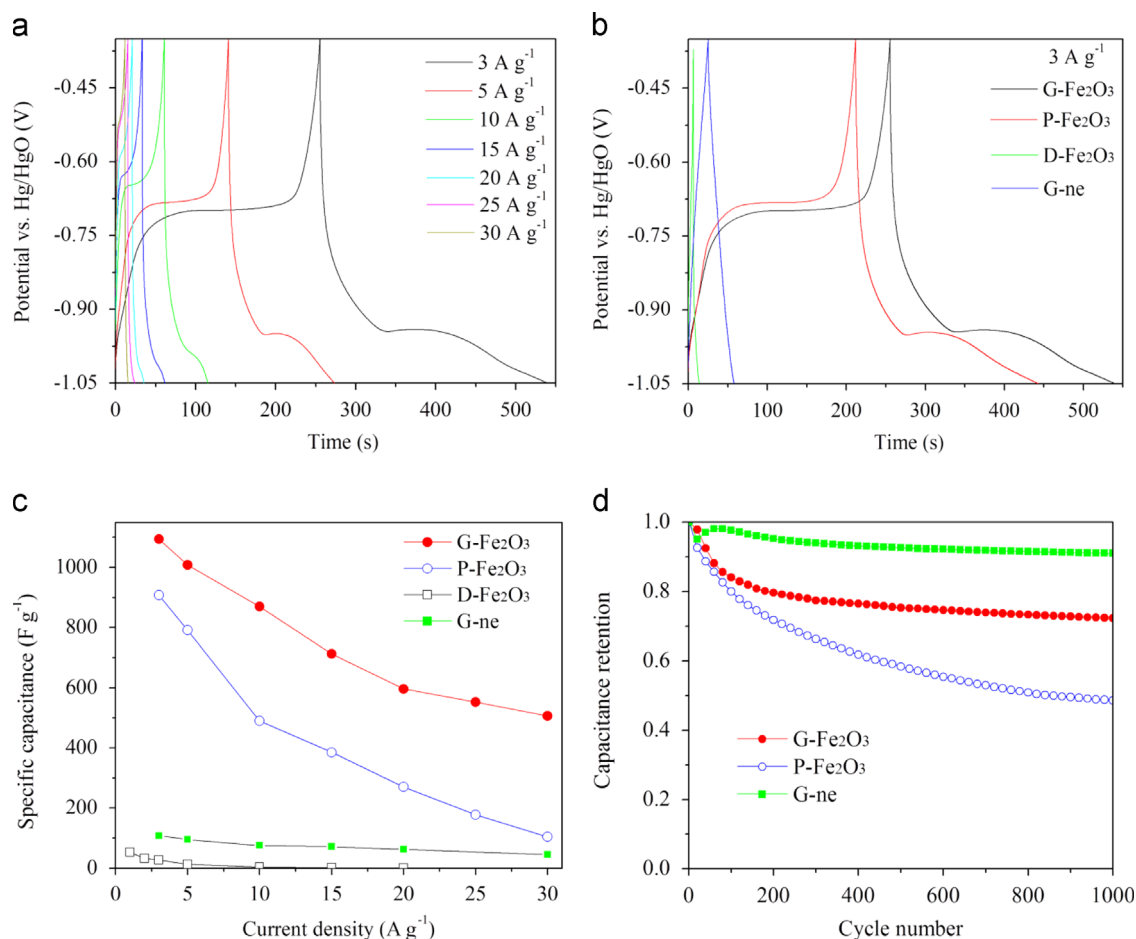


Figure 5 Galvanostatic evaluations in the three-electrode configuration: (a) charging/discharging curves of G- Fe_2O_3 . (b) Comparative galvanostatic curves at 3 A g^{-1} . (c) Comparative specific capacitances measured at various current densities. (d) The evolutions of capacitance retentions versus cycle numbers at 10 A g^{-1} .

Table 1 Specific capacitance of G-Fe₂O₃ versus recently published state-of-the-art Fe-based materials (Fe₂O₃, Fe₃O₄ and FeOOH), all tested in 3-electrode setups.

Active material	Electrolyte	Potential (V)	Capacitance	Ref
G-Fe ₂ O ₃ in this work	3 M KOH	−1.05 to −0.35	1095 F g ^{−1} at 3 A g ^{−1}	
V ₂ O ₅ -doped α-Fe ₂ O ₃ nanotubes	3 M KOH	0.1 to 0.6	135 F g ^{−1} at 3 A g ^{−1}	[51]
Mesh-like Fe ₂ O ₃ /C nanocomposite	2 M KOH	−0.4 to 0.5	~278 F g ^{−1} at 3 A g ^{−1}	[38]
Fe ₂ O ₃ /NrGO hydrogel	1 M KOH	−1.1 to −0.7	~505 F g ^{−1} at 2 A g ^{−1}	[40]
Fe ₃ O ₄ nanoparticles/graphene	1 M KOH	−1 to 0	~250 F g ^{−1} at 3 A g ^{−1}	[52]
Porous α-Fe ₂ O ₃ nanoribbons	1 M KOH	−0.1 to 0.45	~133 F g ^{−1} at 2 A g ^{−1}	[53]
Fe ₂ O ₃ particles/graphene composite	1 M KOH	−1.05 to −0.3	908 F g ^{−1} at 2 A g ^{−1}	[39]
Porous Fe ₃ O ₄ /carbon composite	1 M KOH	−1 to 0	95 F g ^{−1} at 2 A g ^{−1}	[37]
Graphene/Fe ₃ O ₄ nanoparticles	1 M KOH	−1 to 0.1	137.9 F g ^{−1} at 2 A g ^{−1}	[41]
Fe ₃ O ₄ /rGO composite	1 M KOH	−1.1 to −0.1	536.8 F g ^{−1} at 2 A g ^{−1}	[54]
Fe ₃ O ₄ @porous carbon	1 M NaOH	−0.7 to −0.1	126 F g ^{−1} at 1 A g ^{−1}	[55]
α-Fe ₂ O ₃ porous fibers	1 M LiOH	0-0.5	348 F g ^{−1} at 5 A g ^{−1}	[56]
Fe ₃ O ₄ @RGO	1 M LiOH	−1.2 to 0.1	326 F g ^{−1} at 0.5 A g ^{−1}	[47]
Fe ₂ O ₃ nanotubes	5 M LiCl	−0.8 to 0	257.8 F g ^{−1} at 1.4 A g ^{−1}	[11]
α-Fe ₂ O ₃ hollow microspheres	2.5 M Li ₂ SO ₄	−1 to 0	~150 F g ^{−1} at 2 A g ^{−1}	[57]
γ-FeOOH nanosheet	1 M Li ₂ SO ₄	−0.8 to −0.1	310 F g ^{−1} at 1.27 A g ^{−1}	[34]
α-Fe ₂ O ₃ mesocrystals/graphene	1 M Na ₂ SO ₄	−1.2 to −0.2	306.9 F g ^{−1} at 3 A g ^{−1}	[58]
rGO/Fe ₂ O ₃ nanorods	1 M Na ₂ SO ₄	−1 to 0	504 F g ^{−1} at 2 mA cm ^{−2}	[42]
α-FeOOH/Fe ₂ O ₃ nanoparticles	0.1 M Na ₂ SO ₄	0-0.8	160 F g ^{−1} at 5 A g ^{−1}	[59]
Ordered mesoporous carbon/Fe ₂ O ₃	1 M Na ₂ SO ₃	−1.0 to −0.2	~180 F g ^{−1} at 2 A g ^{−1}	[36]
Nanoporous Fe ₃ O ₄ /C nanosheets	1 M Na ₂ SO ₃	−0.8 to −0.2	~160 F g ^{−1} at 2 A g ^{−1}	[60]
Fe ₃ O ₄ nanoparticles	1 M Na ₂ SO ₃	−0.9 to 0.1	106.9 F g ^{−1} at 2 A g ^{−1}	[35]

(ASCs) by employing CoNi-LDH/CNT as the positive electrode material, as illustrated in Figure 6a. In this system, the open circuit potential V_{oc} can reach 1.5-1.7 V with the minimal degree of water split, thanks to the complementary working potential of these two electrode materials. The characterizations and measurements of the CoNi-LDH/CNT electrode are described in Figures S12-S14. The specific capacitance of CoNi-LDH/CNT can reach as high as 1141.1 F g^{−1} at a current density of 3 A g^{−1} and still remains 662.7 F g^{−1} at 30 A g^{−1}. We also have investigated the contribution of Ni foam substrate to the capacitances (see Figure S15) and found it is negligible since we use high mass loadings of active materials. Figures 6 and S16 show electrochemical performances of our ASC device. The CV curves in Figure 6b depict distinct anodic and cathodic peaks through all scan rates, and each paired anodic and cathodic curves are highly symmetric and nearly equal in integrated area, suggesting low polarizations, high electrochemical activities and great reversibilities of both electrode materials. At 5 mV s^{−1}, the difference between redox peaks is 0.40 V, and it increases to 0.48, 0.56, 0.71 and 0.83 V at 10, 20, 50 and 100 mV s^{−1}, respectively. Figure 6c shows galvanostatic curves of the ASC under potential cutoff of 0-1.5 V at different current densities. At 2 A g^{−1}, the average charging and discharging potentials are 1.19 and 0.93 V, respectively. In addition, the average equivalent series resistance (R_{ESR}) calculated on the basis of voltage drops is merely 0.404 Ω cm^{−2}.

The capacitance of the ACS (calculated based on the total mass of the active electrode materials) ranges from 252.4 to 47.3 F g^{−1} when the current density is increased from 0.5 to 50 A g^{−1} (Figure S16b). Ragone plots comparing our ASC with the recently reported state-of-the-art ASCs are displayed in

Figure S16c and further described in Table S1. Our ASC shows the champion performance with the highest energy density up to 98.0 W h kg^{−1} under a power density of 465.9 W kg^{−1}. Even when the power density is increased to 22,861.8 W kg^{−1}, the energy density of our ASC still maintains 9.0 W h kg^{−1} with a discharging time of less than 1.5 s. Given that Figure S16c and Table S1 consider only the mass of the active materials, in Figure 6d we divide those values by four to take into consideration the mass of other supercapacitor components [4]. It can be seen from Figure 6d that our ASC manifests higher energy density than commercial EDLCs and higher power density than Li-ion and lead acid batteries. In terms of cycling stability, our ASC device shows capacitance retention of 78.0% after 1000 cycles (see Figure S16d). Furthermore, the slow self-discharge behavior of the ASC device is verified in Figure S17. To further demonstrate the high energy and high power of the ASC, we connected three coin cells in series and used the tandem device to power nine blue light-emitting diodes (LEDs, ~75 mW each), as shown in Figure S18 and the supplementary video. The LEDs remained lightened up for more than 2 h.

Supplementary material related to this article can be found online at <http://dx.doi.org/10.1016/j.nanoen.2015.05.021>.

Conclusion

In summary, we have demonstrated a scalable approach to produce graphene/porous iron oxide nanocomposite as the anode material for supercapacitors. Benefiting from the highly conductive graphene scaffold augmented with well-dispersed Fe₂O₃ nanostructures, the nanocomposite G-Fe₂O₃ demonstrates

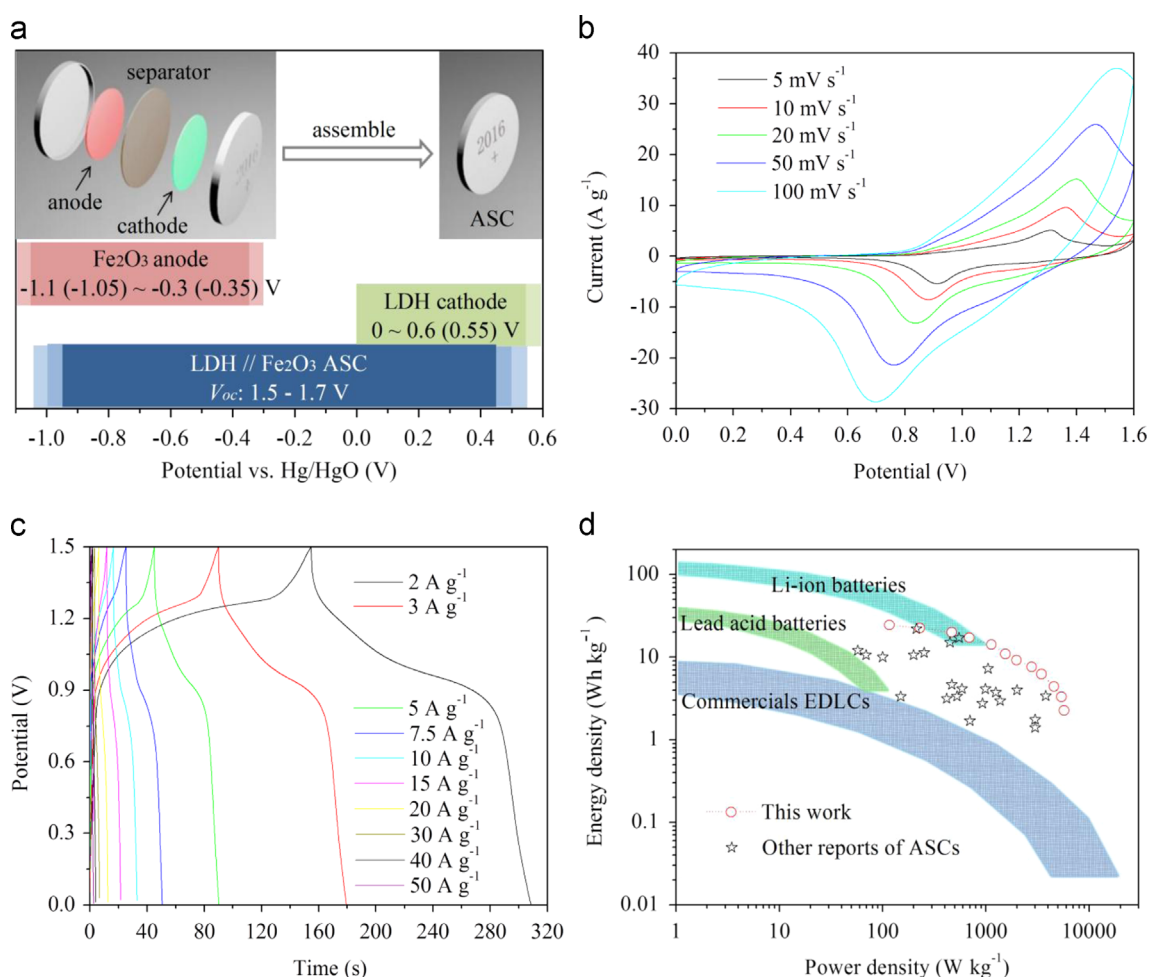


Figure 6 (a) Illustration of assembling full ASC devices. (b) CV curves of the ASC at different scan rates. (c) Galvanostatic curves at different current densities. (d) Ragone plots of energy density versus power density for our ASC device compared with the values reported from other refs marked with stars (note that all the values are divided by a factor of four in consideration of the mass of other components in practical applications).

a very high capacitance of 1095 F g⁻¹ at a current density of 3 A g⁻¹. Furthermore, asymmetric supercapacitors are assembled using G-Fe₂O₃ and CoNi-LDH/CNT as the negative and positive electrode materials, respectively, and exhibit high energy density (up to 98.0 Wh kg⁻¹), high power density (up to 22,826 W kg⁻¹) as well as long-term cycling stability. This study highlights the benefits of controlling nanomorphology to achieve superior electrochemical properties. The material design and characterizations may shed light on the development of new hybrid materials for energy storage applications.

Acknowledgments

This work was supported by Research Grants Council of Hong Kong (General Research Fund, No. 417012, GRC-NSFC, No. N_CUHK450/13, and TRS, No. T23-407/13-N).

Appendix A. Supporting information

Supplementary data associated with this article can be found in the online version at <http://dx.doi.org/10.1016/j.nanoen.2015.05.021>.

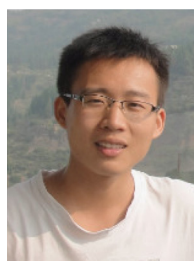
References

- [1] J.R. Miller, P. Simon, *Science* 321 (2008) 651-652.
- [2] P. Simon, Y. Gogotsi, B. Dunn, *Science* 343 (2014) 1210-1211.
- [3] P. Yang, W. Mai, *Nano Energy* 8 (2014) 274-290.
- [4] H. Wang, Z. Xu, A. Kohandehghan, Z. Li, K. Cui, X. Tan, T.J. Stephenson, C.K. King'ondo, C.M. Holt, B.C. Olsen, J. K. Tak, D. Harfield, A.O. Anyia, D. Mitlin, *ACS Nano* 7 (2013) 5131-5141.
- [5] H. Ji, X. Zhao, Z. Qiao, J. Jung, Y. Zhu, Y. Lu, L.L. Zhang, A.H. MacDonald, R.S. Ruoff, *Nat. Commun.* 5 (2014) 3317-3323.
- [6] L.G.H. Staaf, P. Lundgren, P. Enoksson, *Nano Energy* 9 (2014) 128-141.
- [7] M. Sevilla, A.B. Fuertes, *ACS Nano* 8 (2014) 5069-5078.
- [8] D. Puthusseri, V. Aravindan, S. Madhavi, S. Ogale, *Energy Environ. Sci.* 7 (2014) 728-735.
- [9] H. Wang, B. Zhu, W. Jiang, Y. Yang, W.R. Leow, H. Wang, X. Chen, *Adv. Mater.* 26 (2014) 3638-3643.
- [10] L. Yuan, X.H. Lu, X. Xiao, T. Zhai, J. Dai, F. Zhang, B. Hu, X. Wang, L. Gong, J. Chen, C. Hu, Y. Tong, J. Zhou, Z.L. Wang, *ACS Nano* 6 (2012) 656-661.
- [11] P. Yang, Y. Ding, Z. Lin, Z. Chen, Y. Li, P. Qiang, M. Ebrahimi, W. Mai, C.P. Wong, Z.L. Wang, *Nano Lett.* 14 (2014) 731-736.
- [12] J. Xiao, L. Wan, S. Yang, F. Xiao, S. Wang, *Nano Lett.* 14 (2014) 831-838.

- [13] J. Wang, D. Chao, J. Liu, L. Li, L. Lai, J. Lin, Z. Shen, *Nano Energy* 7 (2014) 151-160.
- [14] Z. Li, Z. Xu, H. Wang, J. Ding, B. Zahiri, C.M.B. Holt, X. Tan, D. Mitlin, *Energy Environ. Sci.* 7 (2014) 1708-1718.
- [15] H.B. Li, M.H. Yu, F.X. Wang, P. Liu, Y. Liang, J. Xiao, C.X. Wang, Y.X. Tong, G.W. Yang, *Nat. Commun.* 4 (2013) 1894-1900.
- [16] X. Xiao, Z. Peng, C. Chen, C. Zhang, M. Beidaghi, Z. Yang, N. Wu, Y. Huang, L. Miao, Y. Gogotsi, J. Zhou, *Nano Energy* 9 (2014) 355-363.
- [17] X. Lu, T. Zhai, X. Zhang, Y. Shen, L. Yuan, B. Hu, L. Gong, J. Chen, Y. Gao, J. Zhou, Y. Tong, Z.L. Wang, *Adv. Mater.* 24 (2012) 938-944.
- [18] C. Guan, J. Liu, C. Cheng, H. Li, X. Li, W. Zhou, H. Zhang H.J. Fan, *Energy Environ. Sci.* 4 (2011) 4496-4499.
- [19] Z.-S. Wu, D.-W. Wang, W. Ren, J. Zhao, G. Zhou, F. Li H.-M. Cheng, *Adv. Funct. Mater.* 20 (2010) 3595-3602.
- [20] W. Chen, C. Xia, H.N. Alshareef, *ACS Nano* 8 (2014) 9531-9541.
- [21] L. Shen, Q. Che, H. Li, X. Zhang, *Adv. Funct. Mater.* 24 (2014) 2630-2637.
- [22] C. Zhou, Y. Zhang, Y. Li, J. Liu, *Nano Lett.* 13 (2013) 2078-2085.
- [23] Z. Yu, B. Duong, D. Abbitt, J. Thomas, *Adv. Mater.* 25 (2013) 3302-3306.
- [24] X. Lu, M. Yu, G. Wang, T. Zhai, S. Xie, Y. Ling, Y. Tong, Y. Li, *Adv. Mater.* 25 (2013) 267-272.
- [25] H.W. Shim, A.H. Lim, J.C. Kim, E. Jang, S.D. Seo, G.H. Lee T.D. Kim, D.W. Kim, *Sci. Rep.* 3 (2013) 2325-2333.
- [26] C. Yuan, J. Li, L. Hou, X. Zhang, L. Shen, X.W.D. Lou, *Adv. Funct. Mater.* 22 (2012) 4592-4597.
- [27] Y. Yang, L. Li, G. Ruan, H. Fei, C. Xiang, X. Fan, J.M. Tour, *ACS Nano* 8 (2014) 9622-9628.
- [28] C. Yuan, L. Yang, L. Hou, J. Li, Y. Sun, X. Zhang, L. Shen, X. Lu, S. Xiong, X.W.D. Lou, *Adv. Funct. Mater.* 22 (2012) 2560-2566.
- [29] Z.-S. Wu, G. Zhou, L.-C. Yin, W. Ren, F. Li, H.-M. Cheng, *Nano Energy* 1 (2012) 107-131.
- [30] J. Yan, Z. Fan, W. Sun, G. Ning, T. Wei, Q. Zhang, R. Zhang, L. Zhi, F. Wei, *Adv. Funct. Mater.* 22 (2012) 2632-2641.
- [31] G. Yu, X. Xie, L. Pan, Z. Bao, Y. Cui, *Nano Energy* 2 (2013) 213-234.
- [32] Y. Zhu, X. Ji, C. Pan, Q. Sun, W. Song, L. Fang, Q. Chen C.E. Banks, *Energy Environ. Sci.* 6 (2013) 3665-3675.
- [33] F. Zhang, C. Yuan, J. Zhu, J. Wang, X. Zhang, X.W. Lou, *Adv. Funct. Mater.* 23 (2013) 3909-3915.
- [34] Y.C. Chen, Y.G. Lin, Y.K. Hsu, S.C. Yen, K.H. Chen, L.C. Chen, *Small* 10 (2014) 3803-3810.
- [35] L. Wang, H. Ji, S. Wang, L. Kong, X. Jiang, G. Yang, *Nanoscale* 5 (2013) 3793-3799.
- [36] Y. Lin, X. Wang, G. Qian, J.J. Watkins, *Chem. Mater.* 26 (2014) 2128-2137.
- [37] W. Meng, W. Chen, L. Zhao, Y. Huang, M. Zhu, Y. Huang, Y. Fu, F. Geng, J. Yu, X. Chen, C. Zhi, *Nano Energy* 8 (2014) 133-140.
- [38] B. Sethuraman, K.K. Purushothaman, G. Muralidharan, *RSC Adv.* 4 (2014) 4631-4637.
- [39] H. Wang, Z. Xu, H. Yi, H. Wei, Z. Guo, X. Wang, *Nano Energy* 7 (2014) 86-96.
- [40] Z. Ma, X. Huang, S. Dou, J. Wu, S. Wang, *J. Phys. Chem. C* 118 (2014) 17231-17239.
- [41] Q. Wang, L. Jiao, H. Du, Y. Wang, H. Yuan, *J. Power Sources* 245 (2014) 101-106.
- [42] Q.X. Low, G.W. Ho, *Nano Energy* 5 (2014) 28-35.
- [43] W.S. Hummers Jr, R.E. Offeman, *J. Am. Chem. Soc.* 80 (1958) 1339-1339.
- [44] N.I. Kovtyukhova, P.J. Ollivier, B.R. Martin, T.E. Mallouk S.A. Chizhik, E.V. Buzaneva, A.D. Gorchinskiy, *Chem. Mater.* 11 (1999) 771-778.
- [45] Y. Cheng, B. Zou, C. Wang, Y. Liu, X. Fan, L. Zhu, Y. Wang, H. Ma, X. Cao, *CrystEngComm* 13 (2011) 2863-2870.
- [46] J. Gong, K. Yao, J. Liu, Z. Jiang, X. Chen, X. Wen, E. Mijowska, N. Tian, T. Tang, *J. Mater. Chem. A* 1 (2013) 5247-5255.
- [47] Q. Qu, S. Yang, X. Feng, *Adv. Mater.* 23 (2011) 5574-5580.
- [48] L.-F. Chen, Z.-Y. Yu, X. Ma, Z.-Y. Li, S.-H. Yu, *Nano Energy* 9 (2014) 345-354.
- [49] S. Sun, J. Lang, R. Wang, L. Kong, X. Li, X. Yan, *J. Mater. Chem. A* 2 (2014) 14550-14556.
- [50] J.P. Alper, S. Wang, F. Rossi, G. Salviati, N. Yiu, C. Carraro, R. Maboudian, *Nano Lett.* 14 (2014) 1843-1847.
- [51] G. Nie, X. Lu, J. Lei, Z. Jiang, C. Wang, *J. Mater. Chem. A* 2 (2014) 15495-15501.
- [52] M. Liu, J. Sun, *J. Mater. Chem. A* 2 (2014) 12068-12074.
- [53] D. Sarkar, M. Mandal, K. Mandal, *ACS Appl. Mater. Interfaces* 5 (2013) 11995-12004.
- [54] T.W. Lin, C.S. Dai, K.C. Hung, *Sci. Rep.* 4 (2014) 7274-7283.
- [55] L. You, Y. Zhang, S. Xu, J. Guo, C. Wang, *ACS Appl. Mater. Interfaces* 6 (2014) 15179-15187.
- [56] G. Binitha, M.S. Soumya, A.A. Madhavan, P. Praveen, A. Balakrishnan, K.R.V. Subramanian, M.V. Reddy, S.V. Nair, A.S. Nair, N. Sivakumar, *J. Mater. Chem. A* 1 (2013) 11698-11704.
- [57] L. Xu, J. Xia, H. Xu, S. Yin, K. Wang, L. Huang, L. Wang, H. Li, *J. Power Sources* 245 (2014) 866-874.
- [58] S. Yang, X. Song, P. Zhang, J. Sun, L. Gao, *Small* 10 (2014) 2270-2279.
- [59] R. Barik, B.K. Jena, A. Dash, M. Mohapatra, *RSC Adv.* 4 (2014) 18827-18834.
- [60] D. Liu, X. Wang, X. Wang, W. Tian, J. Liu, C. Zhi, D. He, Y. Bando, D. Golberg, *J. Mater. Chem. A* 1 (2013) 1952-1955.



Jizhang Chen received his B.S. degree in Chemical Engineering and Ph.D. degree in Applied Chemistry from the Shanghai Jiao-tong University in 2009 and 2014, respectively. He is currently a postdoc in the group of Prof. Ching Ping Wong and Prof. Ni Zhao at the Chinese University of Hong Kong. His research interest includes aqueous energy storage devices.



Junling Xu received his B.E. degree from the University of Jinan in 2010 and M.E. degree from the Shandong University in 2012. Now he is a Ph.D. candidate in the Department of Electronic Engineering at the Chinese University of Hong Kong under the supervision of Professor Ching Ping Wong and Professor Ni Zhao. He is currently studying the diffusion/migration process and kinetics of electrode reaction for electrochemical energy storage cells.



Shuang Zhou received her B.S. degree from the Department of Chemistry, Tsinghua University, China. Since 2011, she continued her study on graphene-based electronics and energy storage applications under the supervision of Prof. Ching-Ping Wong and Prof. Ni Zhao, and is now a Ph.D. candidate in the Department of Electronic Engineering, the Chinese University of Hong Kong.



Ni Zhao received her B.Eng. degree from the Tsinghua University and M.S. degree from the McMaster University. In 2008, she received her Ph.D. degree in Physics from the University of Cambridge. From 2008 to 2010 she worked as a postdoctoral research fellow at the Massachusetts Institute of Technology. She joined the Department of Electronic Engineering at the Chinese University of Hong Kong in December 2010. Her

current research interests include optoelectronic, electronic and electrochemical devices based on organic and nanostructured materials.



Ching-Ping Wong received B.S. degree from the Purdue University and Ph.D. degree from the Pennsylvania State University. After that, he was with AT&T Bell Laboratories for many years and became an AT&T Bell Laboratories Fellow. Now he is the Dean of the Faculty of Engineering at the Chinese University of Hong Kong and on a no-pay leave from Georgia Institute of Technology where he is a Regents' Professor and the Charles Smith-

gall Institute Endowed Chair at the School of Materials Science and Engineering. He is also a member of the US National Academy of Engineering and a member of Chinese Academy of Engineering.